PHYSICS

Light-induced charged slippery surfaces

Fang Wang[1]†, Meijin Liu[1]†, Cong Liu[1], Qilong Zhao[1], Ting Wang[2], Zuankai Wang[2]*, Xuemin Du[1]*

Copyright © 2022 The Authors, some rights reserved; exclusive licensee American Association for the Advancement of Science. No claim to original U.S. Government Works. Distributed under a Creative Commons Attribution NonCommercial License 4.0 (CC BY-NC).

Slippery lubricant-infused porous (SLIPS) and superhydrophobic surfaces have emerged as promising interfacial materials for various applications such as self-cleaning, anti-icing, and antifouling. Paradoxically, the coverage/screening of lubricant layer on underlying rough matrix endows functionalities impossible on superhydrophobic surfaces; however, the inherent flexibility in programming droplet manipulation through tailoring structure or surface charge gradient in underlying matrix is compromised. Here, we develop a class of slippery material that harnesses the dual advantages of both solid and lubricant. This is achieved by rationally constructing a photothermal-responsive composite matrix with real-time light-induced surface charge regeneration capability, enabling photocontrol of droplets in various working scenarios. We demonstrate that this light-induced charged slippery surface (LICS) exerts photocontrol of droplets with fast speed, long distance, antigravity motion, and directionally collective motion. We further extend the LICS to biomedical domains, ranging from specific morphological hydrogel bead formation in an open environment to biological diagnosis and analysis in closed-channel microfluidics.

INTRODUCTION

Surfaces provide a ubiquitous interface for mass and energy exchange from nonliving matter to living matter. The past decade has witnessed the increasing advances in two typical interfacial materials, slippery lubricant-infused porous (SLIPS) and superhydrophobic surfaces, owing to their various applications such as self-cleaning (*1*, *2*), dropwise condensation enhancement (*3*), anti-icing (*4*, *5*), and antifouling (*6*–*10*). In particular, the replacement of air pockets by a physical lubricant layer in SLIPS imparts intriguing functionalities including self-healing, anti-icing, anti-evaporation, and antifouling, otherwise impossible on superhydrophobic surfaces even in extreme environments (*1*, *4*–*11*). However, such a lubricant layer also brings unwanted issues. First, the presence of lubricant layer screens the underlying matrix, thereby the structural gradient or surface charge gradient normally manifested on solid surface becomes invalid (*12*, *13*). Second, the existence of lubricant also makes it difficult for active and well-controlled manipulation of liquid/droplet in a stimuli-responsive manner.

The physical screening effect caused by the lubricant layer is nonpreferential for various applications, especially in scenarios where well-controlled manipulation and transport of liquids are preferred (*14*–*16*). Current SLIPS for droplet manipulation relies on the utility of a tunable substrate (*17*) or a changeable lubricant layer (*18*), both of which require gravity to overcome droplet contact line pinning and hence are limited by low speed, short distance, and poor controllability (*1*, *11*, *17*–*21*). Although the introduction of external fields such as light (*22*–*24*), magnetic fields (*25*), and electric fields (*26*, *27*) improves the motion behavior of liquids, these active approaches still suffer from poor performances, undesirable cross-contamination, and short-term reliability (*28*–*32*), thus making them challenging for practical applications, especially in biomedical domains (*10*, *33*).

Here, we develop a new class of slippery material that harnesses dual advantages of both solid and lubricant, imparting light-induced surface charge regeneration in real time and well-controlled droplets in various working scenarios in a remote manner. Different from conventional SLIPS (Fig. 1A), the light-induced charged slippery surface, referred to LICS, consists of three core components including microsized Ga-In liquid metal particles (LMPs) for efficiently converting absorbed light into local heat (*34*); poly(vinylidene fluoride-*co*-trifluoroethylene) [P(VDF-TrFE)] copolymer, owing to its excellent ferroelectric behavior (*35*, *36*); and microstructures coated with a layer of hydrophobized silica nanoparticles (SiO_2 NPs) for trapping lubricant (Fig. 1, B to D). Compared to passive SLIPS (*1*, *3*, *15*, *19*, *20*, *37*) and active photocontrol strategies (*16*, *22*, *23*, *38*–*44*), the LICS demonstrates superior light-induced droplet manipulation, including fast speed (~18.5 mm s^{-1}), long distance (~100 mm), antigravity motion with high spatiotemporal resolution, a large range of droplet volumes (10^{-3} to 1.5×10^3 μl), and high generality to various liquids, even biological liquids such as blood (Fig. 1, E to G, figs. S1 to S4, and movies S1 to S6).

RESULTS

Fabrication of LICS

To fabricate LICS, we first prepared a silicone mold with inverse micropyramidal arrays, followed by filling a preprepared and well-dispersed composite solution of LMPs and P(VDF-TrFE), and then a complete solidification (see Materials and Methods). After peeling the cured film from the mold, a high electric field was applied to enhance the polarization of LMP/P(VDF-TrFE), and hydrophobic SiO_2 NPs were further sprayed to form a porous structure for locking the infused lubricant. The LICS film can be made 15.2 cm in diameter, which exhibits excellent flexibility, uniformity, and integrity as revealed by optical and scanning electron microscopy (SEM) images (Fig. 1C and fig. S5A). Notably, energy-dispersive x-ray spectroscopy (EDS) and scanning Kelvin probe microscopy (SKPM) images show a good dispersion of LMPs within P(VDF-TrFE), owing to the strong electrostatic interactions between the positively charged LMPs and the negatively charged fluorine atoms in the copolymer chains (Fig. 1D and fig. S5, B and C). The LICS is adaptive to both liquid and solid lubricants including silicone oil and paraffin (fig. S6), which eliminates contact line pinning and suppresses biofouling compared to its hydrophobic counterparts (fig. S7A). Various

[1]Institute of Biomedical and Health Engineering, Shenzhen Institute of Advanced Technology (SIAT), Chinese Academy of Sciences (CAS), Shenzhen, P. R. China. [2]Department of Mechanical Engineering, City University of Hong Kong, Hong Kong, P. R. China.
*Corresponding author. Email: zuanwang@cityu.edu.hk (Z.W.); xm.du@siat.ac.cn (X.D.)
†These authors contributed equally to this work.

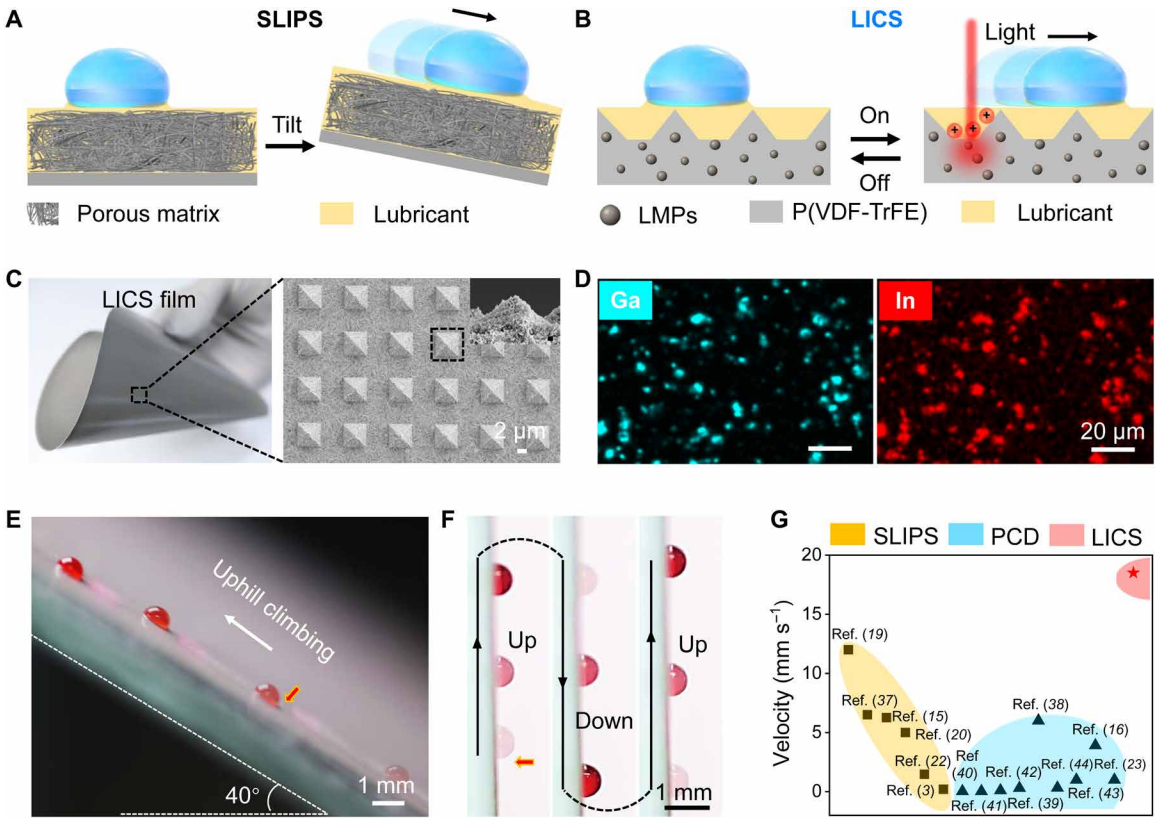

Fig. 1. LICS design. (**A**) Schematic illustration of conventional SLIPS for droplet motion. (**B**) Schematic illustration of LICS for droplet manipulation. (**C**) Photograph of a 15.2 cm 5% LMP/P(VDF-TrFE) composite film and scanning electron microscopy (SEM) images of the film surface patterned with micropyramidal array and a layer of sprayed hydrophobic SiO_2 NPs above the pyramidal. (**D**) Energy-dispersive x-ray spectroscopy (EDS) mapping of Ga-In LMPs embedded in the 5% LMP/P(VDF-TrFE) film. (**E**) Time-lapse trajectory of a 0.23-μl dyed water droplet moving upward on a LICS with a tilting angle of 40° under exposure to near-infrared (NIR; 808 nm) irradiation (100 mW mm^{-2}; movie S3). (**F**) Time-lapse trajectory of a 0.23-μl dyed water droplet moving up and down on a vertically placed LICS (NIR light power density, 100 mW mm^{-2}) (movie S4). (**G**) Comparison of the droplet manipulation performances among the LICS strategy with the reported SLIPS and photocontrol of droplet (PCD).

liquid droplets (4 μl), such as deionized (DI) water, ethylene glycol (EG), glycerol (Gl), tris-buffered saline (TBS) solution, polystyrene latex, and blood, have very low contact angle hysteresis (CAH; <2°). Moreover, the LICS can maintain its repellency for over 30 days without the need of lubricant replenishment (fig. S7B).

Charge regeneration of LICS

When exposing the LICS to near-infrared (NIR) light, the embedded LMPs are capable of efficiently absorbing NIR light and producing a localized temperature rise, which leads to increased thermal movements of P(VDF-TrFE) molecular chains and decreased polarization. Accordingly, the irradiated LICS generates extra positive charges (Fig. 2A and fig. S8). Specifically, in this process, the temperature rise in the irradiated LICS is highly dependent on both the LMP concentration and laser power density as shown in Fig. 2 (B to D). The temperature of 5% LMP/P(VDF-TrFE) film can sharply increase to 40°C in 50 ms under exposure to NIR irradiation of 100 mW mm^{-2}. Figure 2E shows that its light-induced peak-to-peak charge density can rapidly reach as high as 1280 pC mm^{-2} in 0.5 s (fig. S9; see Supplementary Discussion 1.1), which is ~142 times higher than those on superhydrophobic surfaces and large enough to drive droplets (*13*, *45*). Turning off the NIR light irradiation reduces the local temperature and the thermal movements of P(VDF-TrFE) molecular chains, leading to the fast recovery of the P(VDF-TrFE) polarization and disappearance of free surface charges (fig. S10). Notably, the robust charge regeneration capability of LICS shows no apparent decay even after being exposed to 10,000 cycles of impulse NIR irradiation or even immersed with silicone oil for 6 months (Fig. 2F and fig. S11). The light-induced charge regeneration in LICS exhibits superior efficiency, reliability, and stability, eliminating the unwanted screening effect caused by the presence of lubricant.

Mechanism of LICS for droplet manipulation

We next developed a simple model to reveal the mechanism responsible for light-induced droplet manipulation. As schemed in Fig. 3A, bringing a laser spot near to a droplet on a LICS results in a temperature gradient (Fig. 3B) and a nonuniform electric field (Fig. 3C). Thus, the droplet is subject to two forces. First, the temperature gradient generates an internal flow within the droplet and hence a Marangoni force (F_M) with a direction toward the lower temperature side of droplet. On the other hand, the nonuniform electric field gives rise to a dielectrophoretic force (F_e). As shown in Fig. 3D and fig. S12, the maximum F_e occurs near the edge of the laser spot. Here, the magnitudes of F_M and F_e are dictated by the interplay between the spatial locations of the laser spot and droplet or, more quantitatively, by the droplet radius relative to the laser spot width (R/R_0) and the relative position (L). The combined force

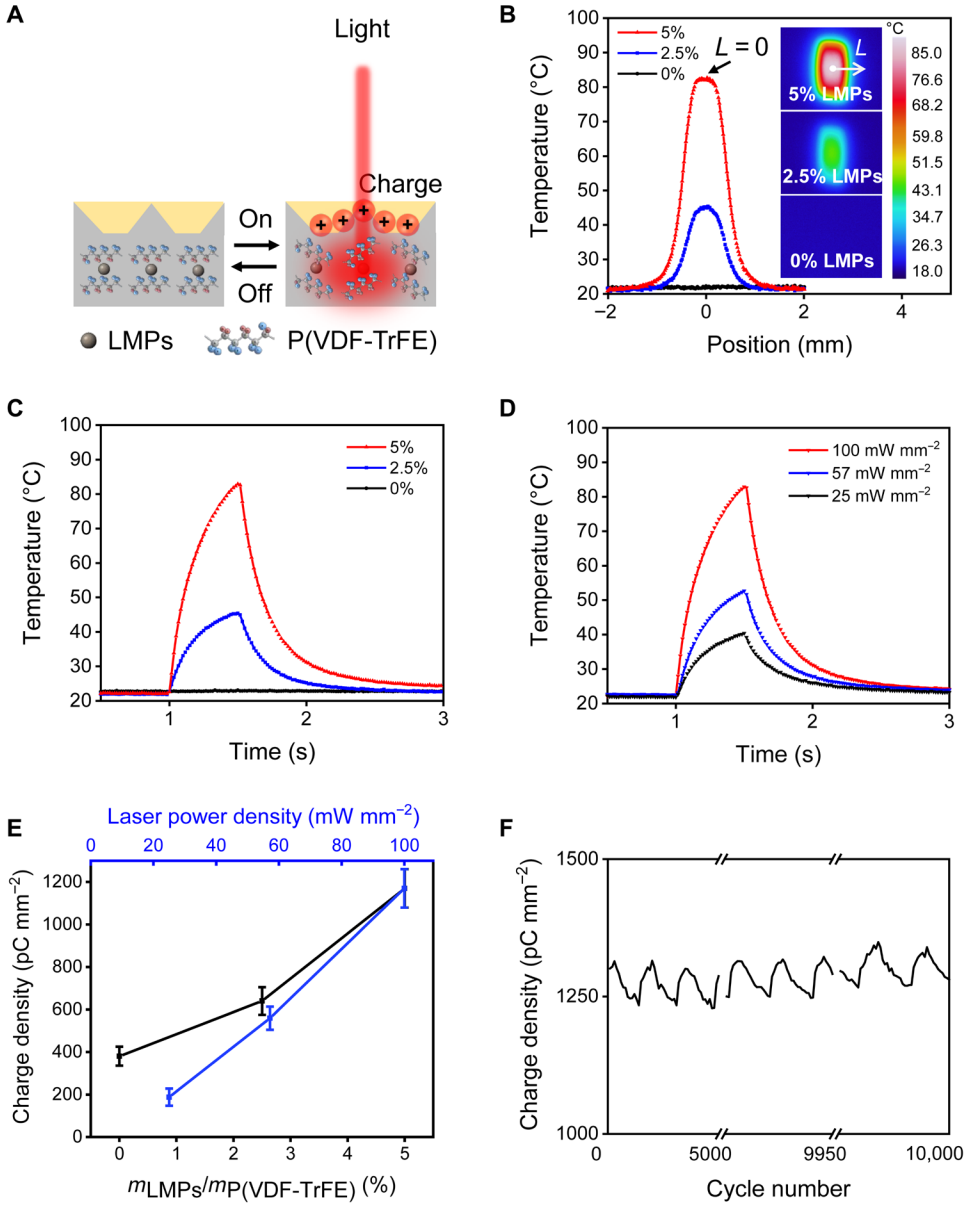

Fig. 2. LICS for charge regeneration. (**A**) Schematic illustration of light-induced free surface charge generation due to the decreased polarization of P(VDF-TrFE) induced by the temperature rise, which is produced by the embedded LMPs. The surface charge generation and disappearance of LICS can be induced by on-off switching of light. (**B**) The temperature distributions of LICS with different concentrations of LMPs (0, 2.5, and 5%) upon exposure to NIR irradiation with a power density of 100 mW mm^{-2} for 0.5 s at room temperature. The inserted infrared thermal images show the temperature gradient along the laser spot center axis direction (*L*). (**C**) The temperature variation of LICS films with different concentrations of LMPs (0, 2.5, and 5%) upon exposure to NIR irradiation with a power density of 100 mW mm^{-2} for 0.5 s at room temperature. (**D**) The temperature variation of a LICS film [5% LMP/P(VDF-TrFE)] upon exposure to NIR irradiation with different power densities (25, 57, and 100 mW mm^{-2}) for 0.5 s at room temperature. (**E**) The charge density increases via increasing the concentration of LMPs in LICS film or the light power density. (**F**) The durability of light-induced charge density of LICS after 10,000 cycles of impulse NIR irradiation with a power density of 100 mW mm^{-2} at a frequency of 0.5-s on and 5-s off at room temperature.

(F_c) is validated by simulations, which show that a droplet can be easily and rapidly attracted to or repulsed away from the laser spot on a LICS due to the light-induced large F_e (Fig. 3D and figs. S13 to S15; see Supplementary Discussion 1.2). In contrast, this is impossible to be achieved on conventional slippery surfaces, owing to the lacking of sufficient surface charges.

Consistent with simulations, our experiments also demonstrate that the droplet behavior on LICS is closely related with $(L - R)/R_0$, a parameter quantifying droplet motion speed and direction (figs. S16 to S27; see Supplementary Discussion 1.2). When $(L - R)/R_0 > 0$, the droplets can be rapidly attracted to the laser spot and have a maximum speed as the front edge of droplet is at the right edge of laser spot [$(L - R)/R_0 \approx 1$]. On the contrary, when $(L - R)/R_0 < 0$, the droplets are repulsed away from the laser spot (Fig. 3E). Even on a LICS with a 35-μm-thick lubricant layer associated with a relatively large viscous resistance, the droplet can still attain a high average

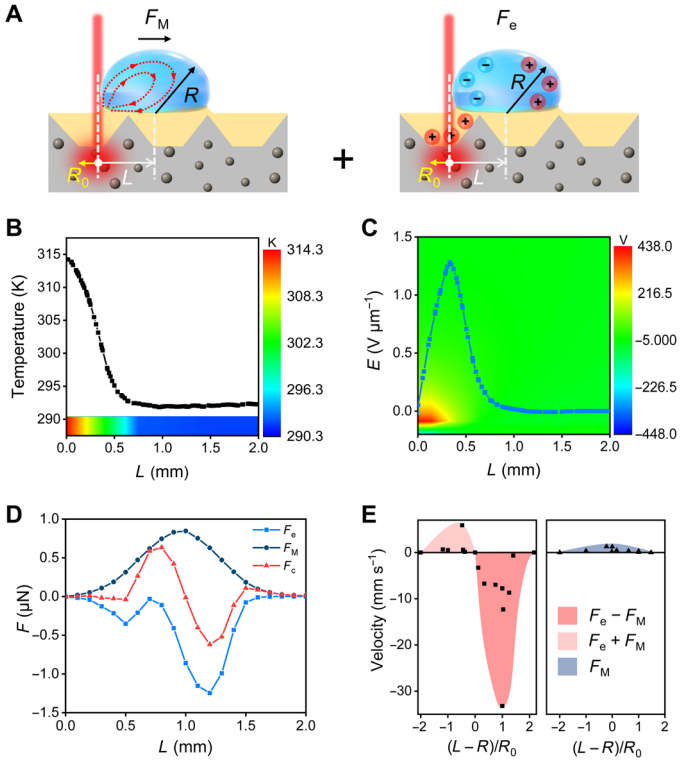

Fig. 3. Mechanism of LICS for droplet dynamics. (**A**) Schematic illustrations of the combined photothermal-induced Marangoni force (F_M) and light-induced dielectrophoretic force (F_e, *L*-direction component) for droplet dynamics on a LICS. *L* is the distance between the laser spot center (*L*-direction width, R_0) and the droplet center (radius, *R*). (**B**) Temperature mapping in LICS is simulated using a finite-element method. (**C**) Electrical field mapping in LICS. The electrical field strength peaks near the edge of the laser spot and decays toward its surroundings. (**D**) The variations of F_M, F_e, and the combined force (F_c; including F_M and F_e) as a function of *L*. (**E**) Phase diagram illustrating the droplet dynamic behaviors on LICS ($F_e - F_M$: attraction to or $F_e + F_M$: repulsion away from the laser spot) and on control slippery film without the capability of light-induced charge generation (F_M: only repulsion away from the laser spot).

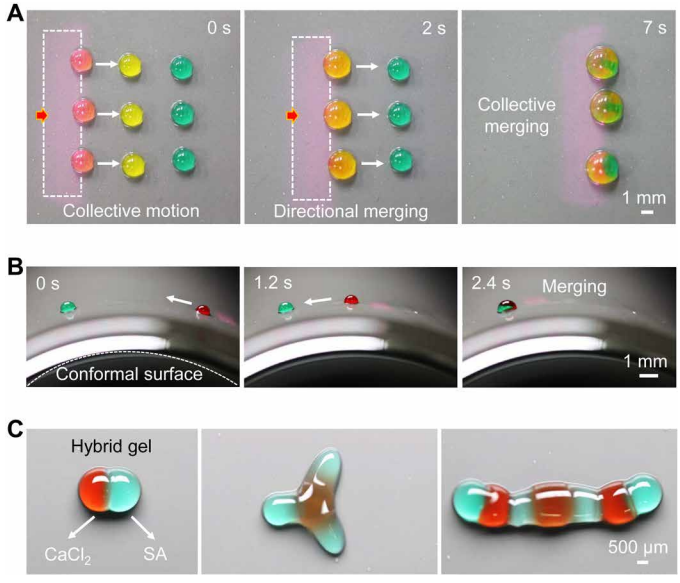

Fig. 4. Open LICS platform for droplet manipulation. (**A**) Photographs of collective motion and directed merging of three 2-μl dyed water droplets when exposed to a single laser beam (12 mW mm^{-2}). (**B**) Side-view photographs of a 0.23-μl water droplet moving on a curved slippery surface (80 m^{-1}) under exposure to NIR irradiation (100 mW mm^{-2}). (**C**) Merging of SA droplets (2 μl, 2.0 wt %, green) and $CaCl_2$ droplets (1 μl, 0.9 M, red) into hydrogel beads with various morphologies on LICS.

velocity (7.4 mm s^{-1}; fig. S28), confirming the dominant effect of dielectrophoretic force. In addition, the droplet remains a constant speed during scanning back and forth for 5 cycles by an NIR laser beam, implying the consistent dielectrophoretic force during the to-and-fro movements (fig. S29). Moreover, the droplet shows a slight temperature variation and negligible evaporation during movement, suggesting that the very short time of NIR irradiation is sufficient to generate the dielectrophoretic force large enough to drive droplets (fig. S30).

Open LICS platform for adaptive droplet manipulation

Aside from the above advantages, the LICS also imparts a new dimension and flexibility in droplet manipulation. First, multiple droplets can be simultaneously controlled by a single laser beam. As shown in Fig. 4A and movie S7, three 2-μl dyed droplets can be driven and then merge with the second and the third row of droplets stepwise under the control of a single laser beam, all of which are otherwise impossible on conventional SLIPS and superhydrophobic surfaces. Second, the LICS platform is highly flexible and can conform onto curved substrates for droplet manipulation including transport and merging (Fig. 4B and movie S8). Third, the LICS also serves as a versatile platform for droplet robotic applications (figs. S31 and S32), including droplet mixing, tiny droplet collection, folding a hydrogel flower (movie S9), and transporting a solid cargo (movie S10). By adding polymerizable moieties into the droplets such as sodium alginate (SA) and calcium chloride ($CaCl_2$), we can prepare biohydrogel beads into various morphologies (Fig. 4C) (*46*).

Leveraging on the photothermal effect, LICS endows the solid paraffin as a lubricant, displaying reversible liquid-solid transitions via increasing/decreasing temperature under exposure to a moving laser, thus inducing rapid droplet motion on both horizontal and vertical LICS (fig. S33 and movies S11 and S12). The utility of the solid-based lubricant also imparts the long-term stability (> 60 days) of the LICS for photocontrol of droplets (fig. S34).

Close LICS platform for bioapplications

One of the biggest bottlenecks restricting practical applications of SLIPS and superhydrophobic surfaces, particularly for biomedical domains, is their limited durability, owing to the presence of undesirable liquid evaporation and cross-contamination on surfaces as well as the difficulty in adopting them into the closed environment (*10*, *33*). Notably, leveraging on the photocontrol, the LICS is naturally suitable to be integrated into a closed system (fig. S35A and movie S13). Figure 5A shows that a microfluidic chip can be facilely constructed by sandwiching a flexible LICS film with two preprepared poly(methyl methacrylate) (PMMA) slides, followed by filling with silicone oil (fig. S35B; see Materials and Methods). The closed LICS chip provides a robust platform for precise and remote photocontrol of a water droplet to cross a maze in the chip, which signifies its light-induced charge regeneration capability (Fig. 5B and movie S14). This unique feature of the LICS chip provides a promising bioanalysis platform to monitor the generation of thrombin

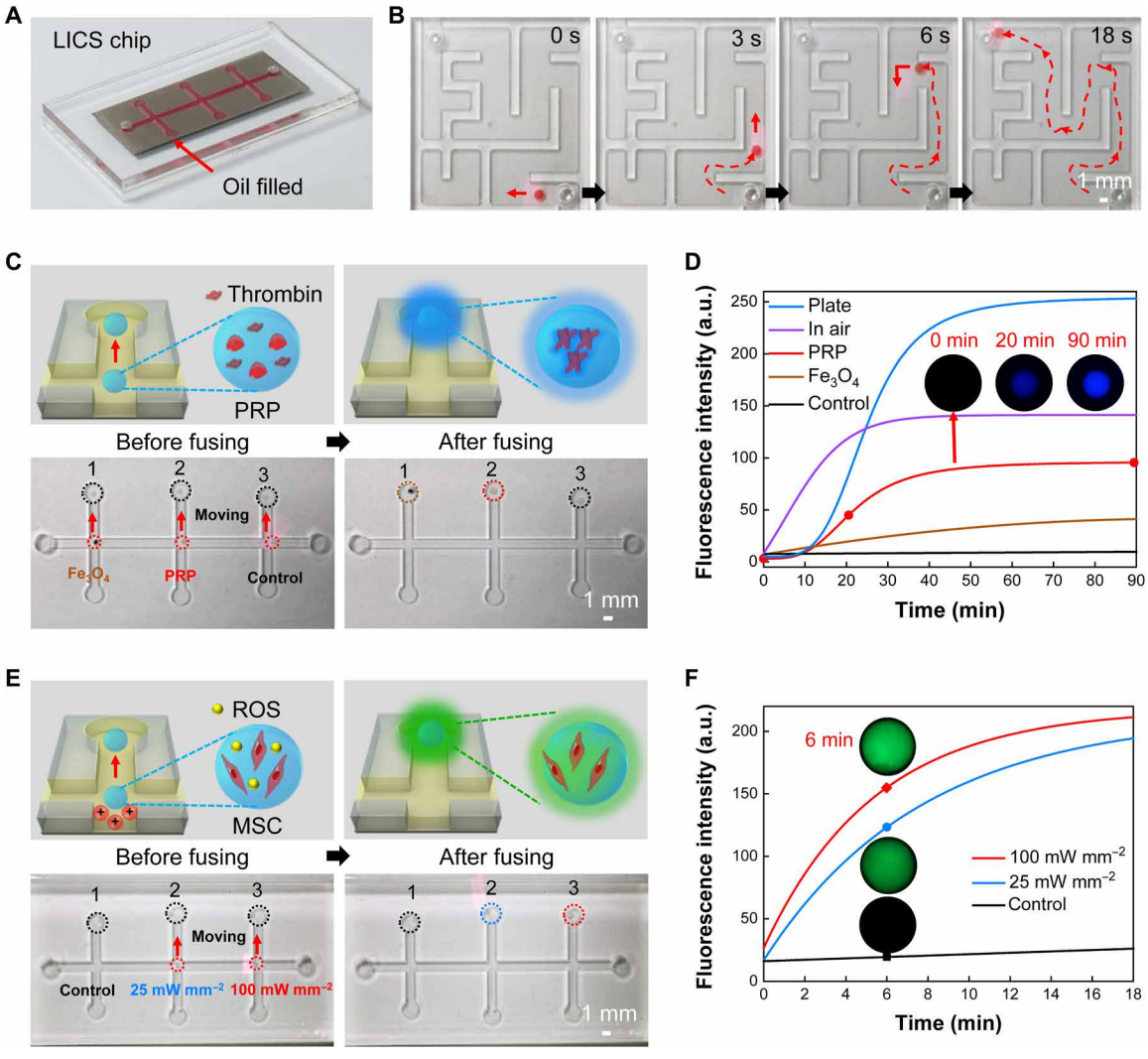

Fig. 5. Closed LICS chip for bioapplications. (**A**) The packed LICS chip filled with dyed silicone oil. (**B**) Photocontrol of a 1-μl water droplet in a microfluidic maze filled with silicone oil. (**C**) Schematic illustrations of photocontrol of droplet with PRP before (top left) and after (top right) fusing with the droplet containing thrombin-sensitive fluorescence probe. Photographs of photocontrol of droplets (200 nl) with Fe_3O_4 particles and PRP, PRP, and PBS as a control before (bottom left) and after (bottom right) fusing with the droplets (200 nl) containing thrombin-sensitive fluorescence probe in wells 1, 2, and 3, respectively. (**D**) The fluorescence intensity and the inserted fluorescence images of the control and compared strategies for blood coagulation analysis. (**E**) Schematic illustrations of photocontrol and in situ electrical stimulation of droplet with MSCs before (top left) and after (top right) fusing with the droplet containing ROS-sensitive fluorescence probe. Photographs of photocontrol and electrical stimulation of droplets (200 nl) with MSCs before (bottom left) and after (bottom right) fusing with the droplets (200 nl) containing a ROS-sensitive fluorescence probe in wells 2 and 3 via a handheld laser with different power densities of 25 and 100 mW mm^{-2}, respectively. (**F**) The fluorescence intensity and the inserted fluorescence images of the control and the cell-fused droplets under NIR irradiation. a.u., arbitrary units.

(Fig. 5, C and D), which is an important indicator of human coagulation functions (*47*, *48*). Briefly, droplets with thrombin-sensitive fluorescence probe were first manipulated into specific wells in the chip, which were then fused with later droplets containing Fe_3O_4 NPs and platelet-rich plasma (PRP), PRP, and control [phosphate-buffered saline (PBS)], respectively (Fig. 5C). Owing to the antibiofouling and antievaporative environment provided by the LICS chip, nanoliter droplets with PRP can be incubated intact at room temperature for 90 min to generate thrombin, which resembles the standard situation in a 96-well plate. On the contrary, adding Fe_3O_4 NPs causes undesirable cross-contamination, and monitoring in the open environment leads to fast evaporation of the tiny droplets, both of which result in unreliable measurements (Fig. 5D and fig. S36).

Notably, the reversible charge generation capability of the LICS also enables in situ stimulation and monitoring of cell responses simultaneously in one chip (Fig. 5, E and F), which plays a vital role in the development of neural tissue engineering and regenerative medicine (*49*). In our experiment, droplets containing a reactive oxygen species (ROS)–sensitive fluorescence probe and mesenchymal stem cells (MSCs) suspension were respectively manipulated and then fused by an NIR laser beam (Fig. 5E). Compared to the control, the fused droplets with MSCs show fast generation and accumulation of cytoplasmatic ROS over time, owing to the electric stimulation during manipulation, which is validated by the increasing fluorescence intensity over time. Notably, the ROS level can be further regulated by varying the NIR light power density during photocontrol

of droplet. On the contrary, the ROS level of the control shows no significant change (Fig. 5F and fig. S37).

DISCUSSION

In summary, we developed a new class of slippery material that harnesses dual advantages of both solid and lubricant, which overcomes the barriers inherent in conventional SLIPS and superhydrophobic surfaces, owing to the robust capability of real-time light-induced charge regeneration with superior efficiency, reliability, and stability. We show that LICS renders photocontrol of droplets with dynamic adaptive functionalities, such as fast speed (~18.5 mm s^{-1}), long distance (~100 mm), antigravity climbing, single-to-multiple droplets, microscale-to-macroscale size (from 10^{-3} to 1.5×10^{3} μl), flat-to-curved surface, and open-to-closed system, otherwise unachievable in current SLIPS. The high reliability, superior stability, and outstanding functionalities of LICS impart the construction of pump-loss microfluidic devices that are contact free, loss free, antievaporative, and antibiofouling. The simple design, portable operation, and unique features of the LICS would open new avenues for the next-generation interfacial materials and microfluidics, bringing wide possibilities for chemical and biomedical applications.

MATERIALS AND METHODS

Materials

P(VDF-TrFE) (70/30 mole percent; weight-average molecular weight, 520,000 to 860,000) copolymer was supplied by Piezotech (Pierre-Benite, France). Sodium chloride (NaCl), SA, $CaCl_2$, EG, Gl, rhodamine 6G, TBS, *1H,1H,2H,2H*-perfluorodecyl trichlorosilane (PFDTS; 96%), and dimethyl sulfoxide (DMSO) were purchased from Aladdin Reagent Co. Ltd. (Shanghai, China). Solid paraffin wax (melting point, 42° to 44°C), chitosan with low average molecular weight, dichlorofluorescein diacetate (DCFDA), bovine serum albumin (BSA), Dulbecco's PBS, and glutaraldehyde aqueous solution [25.0 weight % (wt %)] were purchased from Sigma-Aldrich (Missouri, USA). Liquid metal (LM) eutectic gallium-indium (Ga/In, 75.5%/24.5%) was obtained from Fanyada Electronic Technology Co. Ltd. (Zhenjiang, China). Dimethyl silicone oil (viscosity, 10 cSt) was purchased from Dow Corning (Midland, USA). Methyl cellulose was purchased from Alfa Aesar Chemical Reagent Co. Ltd. (Tianjin, China). Commercial solution of superhydrophobic SiO_2 NPs was purchased from Schanda Chemical Co. Ltd. (Foshan, China). MSCs were obtained from ScienCell (USA). Congo red was purchased from Shanghai Macklin Biochemical Co. Ltd. (Shanghai, China). Acetic acid was obtained from Sinopharm Chemical Reagent Co. Ltd. (Shanghai, China). Magnetic NP solution (Fe_3O_4, 10 to 30 nm, 25% in H_2O) was purchased from the Shanghai Mackin Biochemical Co. Ltd. (Shanghai, China). Z-Gly-Gly-Arg-7-amino-4-methylcoumarin (Z-GGR-AMC) was obtained from Nanjing Leon Biotechnology Co. Ltd. (Nanjing, China). Recombinant human tissue factor (rh-TF) was obtained from Beijing Bersee Science and Technology Co. Ltd. (Beijing, China). All reagents were used without further purification. Indium tin oxide/polyethylene terephthalate (ITO/PET) film (6 ohms) was purchased from Yingkou Opivit New Energy Technology Co. Ltd. (Liaoning, China). Ultrapure water (18.2 megohm·cm) produced from an ELGA PURELAB flex water purification system (High Wycombe, UK) was used throughout this study. Blood was collected from a rabbit, in accordance with the ethical protocol given by Shenzhen Institute of Advanced Technology, Chinese Academy of Sciences. Adult's whole blood was provided by the General Hospital of Shenzhen University with the authorization of the hospital.

Preparation of LMPs

The LMPs were synthesized according to the method described in a previous work (*50*). Typically, 15 mg of methyl cellulose was dissolved in 15 ml of hot water at 80°C. After cooling down to room temperature (22°C), 150 mg of LM was added into the above methyl cellulose aqueous solution. Afterward, the mixture was sonicated using an ultrasound (KQ5200DE, 200 W) in an ice bath for 1 hour. After centrifugation at 10,000 rpm for 10 min, residual methyl cellulose in the suspension was removed. Last, the LMPs dispersed in 30 ml of DMSO with a concentration of 5 mg ml^{-1} was used in the following experiments.

Preparation of slippery films

Briefly, a Si mold with inverse micropyramidal array (3.5 μm in depth, 5.0 μm in width, and 5.0 μm in spacing) was fabricated using photolithography followed by anisotropic chemical wet etching. Afterward, P(VDF-TrFE) mixture solutions (100 mg ml^{-1}) with different concentrations of LMPs [m_{LMPs}:$m_{P(VDF\text{-}TrFE)}$: 0, 2.5, and 5%] were prepared by using DMSO as a solvent, and then 30 ml of preprepared solution was cast into the 15.2 cm Si mold with inverse micropyramidal array and dried at 80°C for 12 hours. After annealing treatment at 130°C for 8 hours in a vacuum oven, the film was peeled off from the Si mold by immersing in water and then dried at room temperature. The resulted films were corona-poled with 22 kV for 25 min at room temperature. Last, the slippery films were prepared by spraying a hydrophobic SiO_2 NP layer onto the film surfaces and then infused with silicone oil or paraffin. The poled slippery films were used in the following experiments unless specifically mentioned.

Electrical property measurement

The electrical properties of the slippery films with silicone oil as the lubricant were measured by using a sandwich structure of ITO/slippery film/ITO/PET at room temperature. First, a 200-nm ITO layer was deposited via sputtering on the smooth side of the P(VDF-TrFE) and LMP/P(VDF-TrFE) composite films at room temperature, respectively. Then, silicone oil was infused into the micropyramidal array side of the ITO-deposited P(VDF-TrFE) and LMP/P(VDF-TrFE) composite films, which were then covered with commercial ITO/PET films. Controlled temperature oscillations were applied to the above homemade device of ITO/slippery film/ITO/PET by 808-nm NIR irradiation with a handheld laser pointer (FU808AD500-BXS22130, SZ laser, 500 mW, Shenzhen Zhonglai Technology Co. Ltd.) using a controlled shutter with on-off pulses of 0.5 s/5 s. Then, the short-circuit current and open-circuit voltage were measured by a digital source meter (Keithley 2470).

Light-induced droplet manipulation

Various droplets on the above slippery films were manipulated by a 808-nm NIR laser pointer (FU808AD500-BXS22130, SZ laser, 500 mW, Shenzhen Zhonglai Technology Co. Ltd.). In addition, a 808-nm NIR laser with a larger laser spot area (FU808AD1000-GD22, SZ laser, 1000 mW, Shenzhen Zhonglai Technology Co. Ltd.) was used in specific scenarios, including 1500 μl of water droplet manipulation, multiple droplet manipulation, and droplet manipulation

on slippery films with paraffin as the lubricant. The above-colored droplets were dyed by food dyes.

LICS chip design and fabrication

First, PMMA substrates (length by width by thickness, 4.5 cm by 2.5 cm by 2 mm and 2.5 cm by 2.5 cm by 2 mm, respectively) with channels (width by depth, 1000 μm by 1000 μm; two through-holes, 1.6 mm in diameter) were fabricated using a computer numerical control engraving and milling machine (JK-DK40, China). Then, the machined PMMA substrates were hydrophobically treated by spraying a commercial solution of hydrophobic SiO_2 NPs onto their surfaces, further treated with air plasma (PDC-M, Suzhou Chemical Instrument Co. Ltd.) for 1 min, and afterward deposited with 0.3 ml of PFDTS in vacuum for 5 hours to decrease the surface energy. Then, superhydrophobic LMP/P(VDF-TrFE) films (length by width by thickness, 4 cm by 2 cm by 100 μm or 2 cm by 2 cm by 100 μm) were sandwiched with the resultant PMMA substrates and the same size blank PMMA substrates, which were lastly sealed with a double side adhesive tape (SG-D02, Suzhou Wenhao Microfluidic Technology Co. Ltd., Suzhou, China). Afterward, silicone oil was added into the channel of the above LICS chips for the following experiments.

Measurements of thrombin generation in chip

To measure the generation of thrombin, PRP was first prepared by centrifuging the citrated blood (3.2 w/v%) at 200*g* and 15°C for 10 min. The collected PRP was then supplemented with 0.5 M $CaCl_2$ aqueous solution at a volume ratio of 9:1 (Liquid A). Meanwhile, fluorogenic substrate Z-GGR-AMC and rh-TF solutions were also prepared, by dissolving Z-GGR-AMC and rh-TF in PBS with supplemented 10.0 v/v% DMSO, 150 mM NaCl, with BSA (60 mg ml^{-1}) to a final concentration of 5 mM and in DI water to a final concentration of 100 nM, respectively. Afterward, the Z-GGR-AMC solution, rh-TF solution, and PBS were mixed at a volume ratio of 1:4:15, resulting in a mixture solution (Liquid B) with a Z-GGR-AMC concentration of 250 nM and an rh-TF concentration of 20 nM. Three droplets of Liquid B (200 nl) were injected into the LICS chip and manipulated by an 808-nm NIR laser to move to predetermined wells of the chip. Droplets (200 nl) of freshly prepared Liquid A, Liquid A with Fe_3O_4 NPs (2.5 mg ml^{-1}), and PBS were then injected into the LICS chip and separately manipulated by the NIR laser to move to different wells and fused with the preset Liquid B droplets. After the fusion of different droplets, the fluorescence images of the compound droplets at an excitation of 390 nm and an emission at 460 nm were captured every 5 min within a duration of 90 min. In control experiments, the measurements by mixing 50 μl of Liquid A and 50 μl of Liquid B in a 96-well plate and 200 nl of Liquid A and 200 nl of Liquid B on an open silicone oil infused LICS film at the air atmosphere were also performed at room temperature. The fluorescence intensities of different compound liquids were analyzed by using a software (ImageJ), and the curves demonstrating the changes of fluorescence intensities of each group over time were plotted.

Measurements of ROS level in chip

Human bone marrow–derived MSCs at the passage 3 were cultured using a supplemented MSC medium (7501, ScienCell) in a humidified incubator (37°C, 5 v/v% CO_2 atmosphere). The confluent MSCs were trypsinized and suspended into a suspension with a volume of 500 μl and a cell density of 5×10^6 cells ml^{-1}. Before injecting two droplets (200 nl) of MSC suspension into a LICS chip full of silicone oil in channels, three droplets (200 nl) containing a ROS-sensitive fluorescence probe (DCFDA, 1 mg ml^{-1}) were first injected and manipulated to arrive three designated wells, respectively. The droplets of MSC suspension were then manipulated by an 808-nm NIR laser beam with different power densities (25 or 100 mW mm^{-2}), which were fused with the prelocated DCFDA-containing droplet in designated wells, respectively. The changes in the fluorescence of the droplets over time in the close LICS chip were monitored under a fluorescence microscope (Ti-U, Nikon).

Characterizations

The LMP/P(VDF-TrFE) films were analyzed by using a field emission SEM (Sigma, Carl Zeiss 300, Germany), SKPM (Asylum Research Cypher S, UK), and EDS (Bruker XFlash 6|60 detector, Germany) to evaluate the morphologies, potentials, and elemental maps, respectively. The laser power density was detected by a Thorlabs PM100D optical power meter equipped with a Thorlabs S425C photodiode sensor (diameter, 25.4 mm; power range, 2 mW to 10 W; wavelength range, 190 nm to 20 μm). The optical images of LMP/P(VDF-TrFE) slippery films and droplet motions were photographed by a digital camera (Canon EOS 7D Mark II, Japan). High-resolution thermal images were obtained with an infrared thermometer (R550Pro, 21 μm, NEC, Japan). The video of photocontrol of EG droplet was taken by a fluorescence microscope (Nikon Ni-U, Japan). The fluorescence images of cells were taken by a fluorescence microscope (Nikon Ti-U, Japan). The thickness of the Nile red–stained silicone oil–infused LICS film was observed by a laser scanning confocal microscope (Nikon A1MP, Tokyo, Japan) with an exciting wavelength of 488 nm. Contact angles (CAs), sliding angles, and CAH measurements were carried out with a CA meter (DSA30, KRÜSS GmbH) under ambient conditions. To measure the CAH and sliding angle, the LICS films were tilted until the droplet started to slide down. Advancing (θ_{Adv}) and receding (θ_{Rec}) CAs were measured by sliding 4-μl droplets on the LICS films with tilting angles less than 10°.

SUPPLEMENTARY MATERIALS

Supplementary material for this article is available at https://science.org/doi/10.1126/sciadv.abp9369

REFERENCES AND NOTES

1. T.-S. Wong, S. H. Kang, S. K. Y. Tang, E. J. Smythe, B. D. Hatton, A. Grinthal, J. Aizenberg, Bioinspired self-repairing slippery surfaces with pressure-stable omniphobicity. *Nature* **477**, 443–447 (2011).
2. M. Liu, S. Wang, L. Jiang, Nature-inspired superwettability systems. *Nat. Rev. Mater.* **2**, 17036 (2017).
3. K.-C. Park, P. Kim, A. Grinthal, N. He, D. Fox, J. C. Weaver, J. Aizenberg, Condensation on slippery asymmetric bumps. *Nature* **531**, 78–82 (2016).
4. P. Kim, T.-S. Wong, J. Alvarenga, M. J. Kreder, W. E. Adorno-Martinez, J. Aizenberg, Liquid-infused nanostructured surfaces with extreme anti-ice and anti-frost performance. *ACS Nano* **6**, 6569–6577 (2012).
5. M. J. Kreder, J. Alvarenga, P. Kim, J. Aizenberg, Design of anti-icing surfaces: Smooth, textured or slippery? *Nat. Rev. Mater.* **1**, 15003 (2016).
6. A. K. Epstein, T.-S. Wong, R. A. Belisle, E. M. Boggs, J. Aizenberg, Liquid-infused structured surfaces with exceptional anti-biofouling performance. *Proc. Natl. Acad. Sci. U.S.A.* **109**, 13182–13187 (2012).
7. S. Sunny, G. Cheng, D. Daniel, P. Lo, S. Ochoa, C. Howell, N. Vogel, A. Majid, J. Aizenberg, Transparent antifouling material for improved operative field visibility in endoscopy. *Proc. Natl. Acad. Sci. U.S.A.* **113**, 11676–11681 (2016).
8. S. Amini, S. Kolle, L. Petrone, O. Ahanotu, S. Sunny, C. N. Sutanto, S. Hoon, L. Cohen, J. C. Weaver, J. Aizenberg, N. Vogel, A. Miserez, Preventing mussel adhesion using lubricant-infused materials. *Science* **357**, 668–673 (2017).

9. C. Howell, A. Grinthal, S. Sunny, M. Aizenberg, J. Aizenberg, Designing liquid-infused surfaces for medical applications: A review. *Adv. Mater.* **30**, 1802724 (2018).
10. J. Li, E. Ueda, D. Paulssen, P. A. Levkin, Slippery lubricant-infused surfaces: Properties and emerging applications. *Adv. Funct. Mater.* **29**, 1802317 (2019).
11. N. Vogel, R. A. Belisle, B. Hatton, T.-S. Wong, J. Aizenberg, Transparency and damage tolerance of patternable omniphobic lubricated surfaces based on inverse colloidal monolayers. *Nat. Commun.* **4**, 2176 (2013).
12. S. Feng, P. Zhu, H. Zheng, H. Zhan, C. Chen, J. Li, L. Wang, X. Yao, Y. Liu, Z. Wang, Three-dimensional capillary ratchet-induced liquid directional steering. *Science* **373**, 1344–1348 (2021).
13. Q. Sun, D. Wang, Y. Li, J. Zhang, S. Ye, J. Cui, L. Chen, Z. Wang, H.-J. Butt, D. Vollmer, X. Deng, Surface charge printing for programmed droplet transport. *Nat. Mater.* **18**, 936–941 (2019).
14. J. R. Millman, K. H. Bhatt, B. G. Prevo, O. D. Velev, Anisotropic particle synthesis in dielectrophoretically controlled microdroplet reactors. *Nat. Mater.* **4**, 98–102 (2004).
15. I. Oh, C. Keplinger, J. Cui, J. Chen, G. M. Whitesides, J. Aizenberg, Y. Hu, Dynamically actuated liquid-infused poroelastic film with precise control over droplet dynamics. *Adv. Funct. Mater.* **28**, 1802632 (2018).
16. J. Wang, W. Gao, H. Zhang, M. Zou, Y. Chen, Y. Zhao, Programmable wettability on photocontrolled graphene film. *Sci. Adv.* **4**, eaat7392 (2018).
17. X. Yao, Y. Hu, A. Grinthal, T.-S. Wong, L. Mahadevan, J. Aizenberg, Adaptive fluid-infused porous films with tunable transparency and wettability. *Nat. Mater.* **12**, 529–534 (2013).
18. K. Manabe, T. Matsubayashi, M. Tenjimbayashi, T. Moriya, Y. Tsuge, K.-H. Kyung, S. Shiratori, Controllable broadband optical transparency and wettability switching of temperature-activated solid/liquid-infused nanofibrous membranes. *ACS Nano* **10**, 9387–9396 (2016).
19. J. Jiang, J. Gao, H. Zhang, W. He, J. Zhang, D. Daniel, X. Yao, Directional pumping of water and oil microdroplets on slippery surface. *Proc. Natl. Acad. Sci. U.S.A.* **116**, 2482–2487 (2019).
20. X. Zhang, L. Sun, Y. Wang, F. Bian, Y. Wang, Y. Zhao, Multibioinspired slippery surfaces with wettable bump arrays for droplets pumping. *Proc. Natl. Acad. Sci. U.S.A.* **116**, 20863–20868 (2019).
21. S. Peppou-Chapman, J. K. Hong, A. Waterhouse, C. Neto, Life and death of liquid-infused surfaces: A review on the choice, analysis and fate of the infused liquid layer. *Chem. Soc. Rev.* **49**, 3688–3715 (2020).
22. C. Gao, L. Wang, Y. Lin, J. Li, Y. Liu, X. Li, S. Feng, Y. Zheng, Droplets manipulated on photothermal organogel surfaces. *Adv. Funct. Mater.* **28**, 1803072 (2018).
23. X. Tang, L. Wang, Loss-free photo-manipulation of droplets by pyroelectro-trapping on superhydrophobic surfaces. *ACS Nano* **12**, 8994–9004 (2018).
24. Z. Wang, Y. Liu, P. Guo, L. Heng, L. Jiang, Photoelectric synergetic responsive slippery surfaces based on tailored anisotropic films generated by interfacial directional freezing. *Adv. Funct. Mater.* **28**, 1801310 (2018).
25. W. Wang, J. V. I. Timonen, A. Carlson, D.-M. Drotlef, C. T. Zhang, S. Kolle, A. Grinthal, T.-S. Wong, B. Hatton, S. H. Kang, S. Kennedy, J. Chi, R. T. Blough, M. Sitti, L. Mahadevan, J. Aizenberg, Multifunctional ferrofluid-infused surfaces with reconfigurable multiscale topography. *Nature* **559**, 77–82 (2018).
26. O. D. Velev, B. G. Prevo, K. H. Bhatt, On-chip manipulation of free droplets. *Nature* **426**, 515–516 (2003).
27. P. Che, L. Heng, L. Jiang, Lubricant-infused anisotropic porous surface design of reduced graphene oxide toward electrically driven smart control of conductive droplets' motion. *Adv. Funct. Mater.* **27**, 1606199 (2017).
28. Z. Yang, J. Wei, Y. I. Sobolev, B. A. Grzybowski, Systems of mechanized and reactive droplets powered by multi-responsive surfactants. *Nature* **553**, 313–318 (2018).
29. X. Liu, N. Kent, A. Ceballos, R. Streubel, Y. Jiang, Y. Chai, P. Y. Kim, J. Forth, F. Hellman, S. Shi, D. Wang, B. A. Helms, P. D. Ashby, P. Fischer, T. P. Russell, Reconfigurable ferromagnetic liquid droplets. *Science* **365**, 264–267 (2019).
30. Y. Zhang, N.-T. Nguyen, Magnetic digital microfluidics-a review. *Lab Chip* **17**, 994–1008 (2017).
31. J. Li, N. S. Ha, R. M. van Dam, Ionic-surfactant-mediated electro-dewetting for digital microfluidics. *Nature* **572**, 507–510 (2019).
32. T. S. Kaminski, P. Garstecki, Controlled droplet microfluidic systems for multistep chemical and biological assays. *Chem. Soc. Rev.* **46**, 6210–6226 (2017).
33. X. Lou, Y. Huang, X. Yang, H. Zhu, L. Heng, F. Xia, External stimuli responsive liquid-infused surfaces switching between slippery and nonslippery states: Fabrications and applications. *Adv. Funct. Mater.* **30**, 1901130 (2020).
34. A. B. M. T. Haque, R. Tutika, R. L. Byrum, M. D. Bartlett, Programmable liquid metal microstructures for multifunctional soft thermal composites. *Adv. Funct. Mater.* **30**, 2000832 (2020).
35. L. Zhang, P. E. Naumov, X. Du, Z. Hu, J. Wang, Vapomechanically responsive motion of microchannel-programmed actuators. *Adv. Mater.* **29**, 1702231 (2017).
36. B. Stadlober, M. Zirkl, M. Irimia-Vladu, Route towards sustainable smart sensors: Ferroelectric polyvinylidene fluoride-based materials and their integration in flexible electronics. *Chem. Soc. Rev.* **48**, 1787–1825 (2019).
37. N. Bjelobrk, H.-L. Girard, S. B. Subramanyam, H.-M. Kwon, D. Quéré, K. K. Varanasi, Thermocapillary motion on lubricant-impregnated surfaces. *Phys. Rev. Fluids* **1**, 063902 (2016).
38. J. Lv, Y. Liu, J. Wei, E. Chen, L. Qin, Y. Yu, Photocontrol of fluid slugs in liquid crystal polymer microactuators. *Nature* **537**, 179–184 (2016).
39. A. Diguet, R.-M. Guillermic, N. Magome, A. Saint-Jalmes, Y. Chen, K. Yoshikawa, D. Baigl, Photomanipulation of a droplet by the chromocapillary effect. *Angew. Chem. Int. Ed.* **48**, 9281–9284 (2009).
40. K. Ichimura, S.-K. Oh, M. Nakagawa, Light-driven motion of liquids on a photoresponsive surface. *Science* **288**, 1624–1626 (2000).
41. G. Kwon, D. Panchanathan, S. R. Mahmoudi, M. A. Gondal, G. H. McKinley, K. K. Varanasi, Visible light guided manipulation of liquid wettability on photoresponsive surfaces. *Nat. Commun.* **8**, 14968–14968 (2017).
42. F. V. Monteleone, G. Caputo, C. Canale, P. D. Cozzoli, R. Cingolani, D. Fragouli, A. Athanassiou, Light-controlled directional liquid drop movement on TiO_2 nanorods-based nanocomposite photopatterns. *Langmuir* **26**, 18557–18563 (2010).
43. M. Yilmaz, H. B. Kuloglu, H. Erdogan, S. S. Cetin, M. S. Yavuz, G. O. Ince, G. Demirel, Light-driven unidirectional liquid motion on anisotropic gold nanorod arrays. *Adv. Mater. Interfaces* **2**, 1500226 (2015).
44. G. L. Liu, J. Kim, Y. Lu, L. P. Lee, Optofluidic control using photothermal nanoparticles. *Nat. Mater.* **5**, 27–32 (2006).
45. Y. Jin, W. Xu, H. Zhang, R. Li, J. Sun, S. Yang, M. Liu, H. Mao, Z. Wang, Electrostatic tweezer for droplet manipulation. *Proc. Natl. Acad. Sci. U.S.A.* **119**, e2105459119 (2022).
46. X. Du, H. Cui, Q. Zhao, J. Wang, H. Chen, Y. Wang, Inside-out 3D reversible ion-triggered shape-morphing hydrogels. *Research* **2019**, 6398296 (2019).
47. S. R. Coughlin, Thrombin signalling and protease-activated receptors. *Nature* **407**, 258–264 (2000).
48. C. H. Hemker, P. L. Giesen, M. Ramjee, R. Wagenvoord, S. Béguin, The thrombogram: Monitoring thrombin generation in platelet rich plasma. *Thromb. Haemost.* **83**, 589–591 (2000).
49. G. Thrivikraman, S. K. Boda, B. Basu, Unraveling the mechanistic effects of electric field stimulation towards directing stem cell fate and function: A tissue engineering perspective. *Biomaterials* **150**, 60–86 (2018).
50. X. Li, M. Li, J. Xu, J. You, Z. Yang, C. Li, Evaporation-induced sintering of liquid metal droplets with biological nanofibrils for flexible conductivity and responsive actuation. *Nat. Commun.* **10**, 1–9 (2019).
51. C. Rinaldi, H. Brenner, Body versus surface forces in continuum mechanics: Is the Maxwell stress tensor a physically objective Cauchy stress? *Phys. Rev. E* **65**, 036615 (2002).
52. A. Benselama, P. Pham, E. Canot, Modeling of the dielectrophoretic forces acting upon biological cells: A numerical comparison between Finite Element/Boundary Element Maxwell stress tensor methods and point–Dipole approach. *NSTI-Nanotech* **1**, 188–191 (2004).
53. F. Peters, D. Arabali, Interfacial tension between oil and water measured with a modified contour method. *Colloids Surf. A Physicochem. Eng. Aspects* **426**, 1–5 (2013).
54. H. Hu, C. Huang, M. Galluzzi, Q. Ye, R. Xiao, X. Yu, X. Du, Editing the shape morphing of monocomponent natural polysaccharide hydrogel films. *Research* **2021**, 9786128 (2021).

Acknowledgments: A special thank you is given to M. Qiu of the General Hospital of Shenzhen University for the provision of adult's blood. We also thank H. Liang and B. Chu from University of Science and Technology of China and X. Jiang from Nanjing University for valuable discussions and suggestions. **Funding:** We acknowledge the financial support provided by the National Key R&D Program of China (2017YFA0701303); the National Natural Science Foundation of China (52022102); the Youth Innovation Promotion Association of CAS (2019353); the Guangdong Regional Joint Fund-Key Project (2021B1515120076); the University Research Council (11213320); the CAS Key Laboratory of Health Informatics, Shenzhen Institutes of Advanced Technology (2011DP173015); and the Fundamental Research Program of Shenzhen (JCYJ20180507182051636 and KQJSCX20180330170232019).
Author contributions: X.D. conceived the idea. X.D., F.W., and M.L. designed the experiments. F.W. and M.L. conducted the experiments. C.L. and T.W. took KPFM images and conducted the finite element analysis. F.W. and Q.Z. performed the biological microassays. X.D. supervised the study. X.D. and Z.W. analyzed the results and wrote the manuscript. All authors contributed to the discussion and interpretation of the results. **Competing interests:** The authors declare that they have no competing interests. **Data and materials availability:** All data needed to evaluate the conclusions in the paper are present in the paper and/or the Supplementary Materials.

Submitted 8 March 2022
Accepted 24 May 2022
Published 8 July 2022
10.1126/sciadv.abp9369